

# OBSERVATIONS OF ABELL 4059 WITH THE *CHANDRA X-RAY OBSERVATORY*, *HUBBLE SPACE TELESCOPE* AND *VERY LARGE ARRAY*: UNRAVELING A COMPLEX CLUSTER/RADIO-GALAXY INTERACTION

YUN-YOUNG CHOI<sup>1,2,3</sup>, CHRISTOPHER S. REYNOLDS<sup>4</sup>, SEBASTIAN HEINZ<sup>5,6,7</sup>, JESSICA L. ROSENBERG<sup>8</sup>,  
ERIC S. PERLMAN<sup>9</sup>, JONGMANN YANG<sup>1,2</sup>

<sup>1</sup>Department of Physics and CSST, Ewha University, Seoul 120-750, Korea

<sup>2</sup>Center for High Energy Physics, Kyungpook National University, Daegu 702-701, Korea

<sup>3</sup>JILA, Campus Box 440, University of Colorado, Boulder CO 80309

<sup>4</sup>Dept. of Astronomy, University of Maryland, College Park, MD 20742

<sup>5</sup>Max-Planck-Institut für Astrophysik, Karl-Schwarzschild-Str. 1, 85740 Garching, Germany

<sup>6</sup>Center for Space Research, Massachusetts Institute of Technology, 77 Massachusetts Avenue, Cambridge, MA 02139

<sup>7</sup>Chandra Fellow.

<sup>8</sup>CASA, Campus Box 389, University of Colorado, Boulder CO 80309

<sup>9</sup>Dept. of Physics, University of Maryland Baltimore County, 1000 Hilltop Circle, Baltimore, MD 21250

*Draft version November 3, 2018*

## ABSTRACT

We present a detailed reanalysis of *Chandra X-ray Observatory* data for the galaxy cluster Abell 4059 and its central radio galaxy, PKS2354–35. We also present new 1.4 GHz and 4.7 GHz CnB-array radio data from the *Very Large Array*<sup>a</sup>, as well as a short archival WFPC2 image from the *Hubble Space Telescope*. The presence of a strong interaction between this radio galaxy and the intracluster medium (ICM) was suggested by Huang & Sarazin (1998) on the basis of a short observation by the *High Resolution Imager* on *ROSAT*, and confirmed in our preliminary analysis of the *Chandra/ACIS-S* data. In particular, X-ray imaging clearly shows two cavities within the ICM that are *approximately* aligned with the radio-galaxy axis. However, using our new radio maps (which are at lower frequencies and better matched to searching for  $\sim 1$  arcmin structures than the previous high-quality maps) we fail to find a detailed correspondence between the  $\sim 1$  arcmin scale radio-lobes and the ICM cavities. This suggests that the cavities are “ghosts” of a previous burst of powerful activity by PKS 2354-35. This is supported by detailed, spatially-resolved, X-ray spectroscopy which fails to find any shock-heated ICM, suggesting that the cavities are evolving subsonically. We also examine the nature of the central asymmetric ridge (or bar) of X-ray emission extending for  $\sim 30$  kpc south-west (SW) of the cluster center that has been noted in these previous analyzes. We find the ridge to be denser and cooler than, but probably in pressure balance with, its surroundings. The thermal evolution of this structure seems to be dominated by radiative cooling, possibly enhanced by the radio-galaxy ICM interaction. We discuss several possible models for the formation of this SW ridge and find none of them to be entirely satisfactory. In our preferred model, the SW ridge is due to radiative cooling induced by an interaction between a radio-galaxy driven disturbance and a pre-existing bulk ICM flow. The presence of such a bulk flow (with a velocity of  $\sim 500$  km s<sup>-1</sup> projected on the plane of the sky) is suggested by the off-center nature of the pair of X-ray cavities. Such a bulk flow can be created during a cluster/sub-cluster merger — the presence of a prominent dust-lane in the cD galaxy of Abell 4059, ESO 349-G010, is circumstantial evidence for just such a merger.

<sup>a</sup>The VLA is part of the National Radio Astronomy Observatory which is a facility of the National Science Foundation operated under cooperative agreement by Associated Universities, Inc.

*Subject headings:* galaxies:jets, galaxies:clusters:individual (Abell 4059), X-rays: galaxies: clusters

## 1. INTRODUCTION

There is an increasing realization that the core regions of clusters of galaxies are complex and dynamic environments. For some time now, it has been argued on the basis of data from imaging X-ray telescopes that the hot intracluster medium (ICM) of the core regions of rich clusters is radiatively-cooling on timescales shorter than the age of the cluster. This gives rise to the phenomenon known as a cooling flow. Fabian (1994) gives an extensive review of cooling flows up to and including constraints from the *ROSAT* observatory. Prior to the launches of the *Chandra X-ray Observatory* and *XMM-Newton*, the X-ray data strongly argued for the inhomogeneous cooling flow model in which gas in cluster cores cools from X-ray emitting

temperatures down to unobservable temperatures as part of a multi-phase ICM over a spatially distributed region of the cluster core. An obvious mystery, and a strong hint that the real situation is more complex, was the lack of cool gas (including significant star formation) observed at other wavebands.

Not surprisingly, the X-ray view of cluster cores became appreciably more complicated with the launch of *Chandra* and *XMM-Newton*. With the very high dispersions possible using the reflection grating spectrometer (RGS) on *XMM-Newton*, detailed emission line spectroscopy of cluster cores became possible for the first time. Using these techniques, observations of Abell 1795 (Tamura et al. 2001) and Abell 1835 (Peterson et al. 2001) both revealed clear evidence for gas cooling from the virial temperature  $kT > 4$  keV down to 1–2 keV. In partic-

ular, one could isolate and identify the L-shell emission lines of iron corresponding to gas spanning this temperature range. However, very tight upper limits were set on the amount of gas below 1–2 keV which were in strong disagreement with the standard cooling flow model. In other words, there is evidence for gas cooling from the virial temperature down to 1–2 keV, whence it disappears. This result has been generalized to a sample of clusters by Peterson et al. (2003). The explanation for the temperature floor is still far from clear. Strong (i.e., order of magnitude) metallicity inhomogeneities will skew the apparent cooling function such that gas below 1 keV cools extremely rapidly, thereby eluding detection (Fabian et al. 2001). However, it is not known how such inhomogeneities will be formed or maintained. Thermal conduction and the action of a central radio galaxy may also be important in producing these temperature floors (Fabian, Voigt & Morris 2002; Voigt et al. 2002; Ruszkowski & Begelman 2002).

In addition to spectral complexity, *Chandra* has revealed that many clusters possess morphological complexities that are thought to arise due to the interaction of the ICM with a central radio galaxy. In some cases, the association is clear. For example, Perseus A (Fabian et al. 2000), Hydra A (McNamara et al. 2000; David et al. 2001; Nulsen et al. 2002), Abell 2052 (Blanton et al. 2001), and Cygnus A (Smith et al. 2001) all show well defined cavities in the X-ray emitting gas which are coincident with the current radio lobes of the central radio galaxy. In these sources, it is clear that the radio lobes have displaced the X-ray emitting gas producing the observed X-ray/radio anti-coincidence.

*Chandra* has also revealed the presence of “ghost” cavities, i.e., X-ray cavities that are *not* coincident with the active radio lobes. Examples include the outer cavity of Perseus A (Fabian et al. 2000), Abell 2597 (McNamara et al. 2001), NGC 4636 (Jones et al. 2002), and Abell 4059 (Heinz et al. 2002). In these sources, it is believed that the cavities are associated with old radio lobes (related to previous cycles of AGN activity). The low-frequency (74 MHz) synchrotron radio emission expected within this scenario from these old radio lobes has been observed from the ghost cavity of Perseus-A (Fabian et al. 2002).

Collectively, these observations give rise to several questions. Most hydrodynamic models for the formation of these cavities (e.g., Clarke et al. 1997; Heinz, Reynolds & Begelman 1998; Reynolds, Heinz & Begelman 2001; Reynolds, Heinz & Begelman 2002, and references therein) involve the pressure-driven growth of a shock-bounded cocoon. However, in almost all cases (with NGC 4636 being a notable exception; Jones et al. 2002), the X-ray shells that bound the observed cavities are cooler than the ambient ICM, seemingly at odds with the shock scenario. It is plausible that the cool shell arises due to the “lifting” of lower-entropy material from the cluster core by the radio galaxy activity (Böhringer et al. 1995; Reynolds et al. 2001; Nulsen et al. 2002), but we would still expect to see some fraction of the sources in the shock-bounded phase. More generally, we need to assess the implications of such data for models of radio galaxy evolution. To achieve this goal requires the detailed analysis of more *Chandra* data together with directed numerical simulations.

Abell 4059 was one of the first clusters known to possess X-ray cavities on the basis of data from the *ROSAT* high-resolution imager (Huang & Sarazin 1998). These cavities were approximately coincident with the radio lobes of the FRI radio galaxy PKS 2354–35, which is hosted by the cD galaxy at the center of the cluster. Huang & Sarazin (1998) also noted an interesting

bar-like feature in the central regions of the cluster perpendicular to the radio axis. The *Chandra* Advanced CCD Imaging Camera (ACIS) observation of this cluster has been previously described by us in Heinz et al. (2002). In that paper, it was shown that the coincidence between the radio lobes and the X-ray cavities is not exact, leading to the conclusion that these are actually “ghost” cavities. It was also suggested that the complex X-ray morphology (including the central bar) arises from an interaction of a radio-galaxy driven expanding cocoon and a pre-existing bulk ICM flow. Such an ICM flow may result from the accretion of a galaxy group by the cluster.

In this paper, we present a detailed reanalysis of the *Chandra*-ACIS observation of the core regions of Abell 4059. We present a spatially-resolved spectral study of the core regions of this cluster. We also present new 1.4 GHz and 4.7 GHz radio data from the Very Large Array (VLA) taken with the CnB configuration, thereby providing a better match providing a better match to the typical spatial scales characterizing the X-ray cavities. We confirm that the arcmin scale radio lobes indeed do not coincide precisely with the X-ray cavities, especially to the south-east of the center. We also find that the ridge of emission to the SW of the center is cooler and denser, but probably in pressure equilibrium, with the surrounding ICM. Furthermore, it is determined that the thermal evolution of this structure must be dominated by radiative cooling. We discuss various models for the SW ridge, but prefer an explanation in which it corresponds to shock/compression induced cooling of ICM caused by interaction of the radio-galaxy driven disturbance with a bulk ICM flow — however, such a model may suffer fine tuning problems. Finally, we also present an archival *Hubble Space Telescope* (HST) Wide Field Planetary Camera 2 (WFPC2) image of the cD galaxy ESO 349–G010. The presence of a significant dust lane in this elliptical galaxy suggests that it has accreted a gas rich companion galaxy within the past  $\sim 10^8$  yrs. This provides further circumstantial evidence for the putative cluster/group merger required to produce the bulk ICM flow. Section 2 details the *Chandra*, VLA and HST data reduction, and Section 3 describes our imaging and spectroscopy investigations. The observational results are summarized, and possible models discussed, in Section 4.

Throughout this paper we assume  $H_0 = 65 \text{ km s}^{-1} \text{ Mpc}^{-1}$  and  $q_0 = 0.5$ . Given a redshift of  $z = 0.049$ , this cosmology places PKS 2354–35 and Abell 4059 at a luminosity distance of 226 Mpc.

## 2. OBSERVATIONS AND BASIC DATA REDUCTION

### 2.1. X-ray Observations (*Chandra*)

A4059 was observed by *Chandra* for 24.6 ksec on September 24, 2000 and for 20.1 ksec on January 4, 2001, using the ACIS detector. The central radio source, PKS 2354–35, was centered 1 arcmin from the aim point on the S3 back-illuminated ACIS chip (7) such that the core of the cluster could be imaged entirely by the S3 chip. Here, we analyze data from this chip only. The data were filtered so as to include only events with ASCA grades 0,2,3,4, and 6. The gain for the first observation was reprocessed using `acis_process_events` with the latest version of the gain file appropriate for data taken with a focal-plane temperature of  $-120^\circ\text{C}$  (`acisD2000-08-12gainN0003.fits`). Some periods during the first observation were affected by background flares. These were removed by excluding all times for which the background rate exceeded the quiescent rate by

a factor of 1.2. This left a total exposure time of 10.1 ksec and 17.7 ksec for the two observations, respectively. Using the blank sky background fields of the same part of the detector we created a background image and spectrum for each observation. Each background dataset was processed using the same gain file in the A4059 observation and the aspect solutions of each observation were applied to the background dataset. All ACIS data reduction was performed using the *Chandra Interactive Analysis of Observations* (CIAO) version 2.2.1, and spectral analysis was performed using the XSPEC fitting package. CIAO 2.2.1 uses Calibration Database (CALDB) version 2.12.

For both imaging and spectral analyzes, we did *not* use the overall merged event list for the two observations since it does not contain a valid aspect solution. This would lead to slight errors in the corresponding exposure maps and insufficient information to build correct Response Matrix Files (RMFs) and Ancillary Response Files (ARFs). Therefore, for imaging analysis, we also generated separate flux-calibrated images for each observation and then combined them to produce a final image. To produce an image giving the integrated flux over the full 0.3 – 8 keV band, we first computed flux-corrected images in several narrow energy bands and then summed those flux-calibrated images. This is necessary since the effective area of the telescope is both energy and position dependent. To do this, we built several exposure maps which were weighted according to both photoelectric absorption and hot diffuse gas emission models for the incident source spectrum and therefore make it possible to compute the correct surface brightness having less significant spectral variation over the entire image. For spectral analysis, we generated separate source and background spectra (together with the corresponding RMF and ARF files) for each of the two observations and then analyzed them simultaneously. These data reduction steps were facilitated using the CIAO threads provided by the Chandra Science Center.

Astrometric information was obtained directly from the aspect solution provided with the *Chandra* data release. There are two sources in the *Chandra* data that can be clearly identified in other datasets that have accurate astrometry. Firstly, the brightest of the small-scale peaks in the centralmost regions of A4059 lie within 0.5 arcsec of the radio core of PKS2354-35. Secondly, a bright X-ray source to the east of the cluster center lies within 1 arcsec of the 2MASS source 2MASXJ23570418-3448121. Thus, we conclude that the absolute *Chandra* astrometry for this observation is correct to within 1 arcsec.

## 2.2. Radio Observations (VLA)

The pre-existing high-quality radio maps of PKS 2354-35 were taken with the VLA in its A- and B-array configurations at 8.5 GHz and 4.8 GHz (Taylor et al. 1994). Such maps may well miss low surface brightness structure on the arcmin scale, such as could exist within the observed X-ray cavities of A 4059. With this motivation, we obtained new VLA data optimized to study structures on the size scale of the X-ray cavities. In detail, we made continuum flux maps of PKS 2354-35 using the VLA-CnB configuration at 6 and 20 cm. We observed PKS 2354-35 for 37 minutes at C-band with a 50 MHz bandwidth centered at  $\nu = 4.7351$  GHz and for 31 minutes at L-band with a 50 MHz bandwidth centered at  $\nu = 1.4149$  GHz. PKS 2354-35 is a southern source at  $\delta = -34^{\text{h}}45^{\text{m}}30^{\text{s}}$  hence the use of the northern extension, CnB. We were not able to make polarization maps from these data because the restricted time range over which the observations were made meant that no polarization calibrators were available. These VLA data were reduced us-

ing standard AIPS methods. The resultant clean beams for natural weighted maps are fairly elongated: the L-band (1.4 GHz) beam had a major axis of  $20.3''$  and a minor axis of  $14.5''$  while the major axis of the C-band (4.7 GHz) beam was  $6.2''$  and the minor axis was  $4.0''$ .

## 2.3. Optical Observations (HST)

The HST-WFPC2 observed PKS 2354-35 on 2001 April 19 as part of snapshot proposal 8683 (PI: R. van der Marel). The observations were performed in the F814W (broad I) band and the exposure time was 500 seconds, split into two to allow the elimination of cosmic rays. The HST data were retrieved from the public archive and combined using the IRAF/STSDAS task MKDARK, which also allows the elimination of cosmic rays. The data were then rotated to a north-up orientation using the IRAF task IMLINTRAN and registered using WCS information in the header. We examined both the high-resolution ( $0.0455''/\text{pix}$ ) PC image (on which the host galaxy of PKS 2454-35 lies) as well as the four-chip mosaic, which was assembled at  $0.09965''/\text{pix}$  using the IRAF/STSDAS task WMO-SAIC.

## 3. IMAGE ANALYSIS

### 3.1. X-ray morphology

For each of the two *Chandra* observations, the 0.3–8 keV data have been background subtracted and corrected for detector and vignetting effects using weighted exposure maps (see §2). The resulting processed images were then combined. Fig. 1 shows contours of the adaptively smoothed *Chandra* image overlaid on the optical image (from the Digitized Sky Survey) of the cluster. The adaptively smoothed image was derived by smoothing the raw image with a minimum significance of  $4\text{-}\sigma$  using the CIAO tool `csmooth`.

It can be seen that the cluster core has a complex X-ray morphology. The principal morphological features present in these images were previously noted by Huang & Sarazin (1998) and Heinz et al. (2002). The cluster within about  $30''$  radius has an hour-glass like structure (or bar) with two broad peaks. The strongest peak, at the center of the cluster, contains further substructure with 3 bright regions. The brightest region coincides with the optical nucleus (ESO 349-G010 from the Digitized Sky Survey), although it is clearly not a point source. In fact, we do not detect any pointlike source coincident with the nucleus of PKS 2354-35. The second of the principal X-ray peaks is  $\sim 15''$  south-west from the center has no optical or radio counterpart. The SW edge of this feature is so sharp as to be unresolved in our adaptively smoothed map; more precisely, inspection of the smoothing length map produced by `csmooth` indicates that the SW edge of this feature must be less than 3-4 arcsec (3-4 kpc) across. On larger scales, the X-ray emission is elongated and aligned along almost the same position angle as the major axis of the cD galaxy.

Furthermore, there are two cavities in the X-ray emission to the NW and SE of the cluster center (see Heinz et al. 2002 for a detailed discussion of the statistical significance of these cavities). The NW cavity seen in our *Chandra* data can clearly be identified with the NW cavity seen in the ROSAT-HRI data. For the more subtle SE cavity, however, the *Chandra* cavity appears in a different position by about  $20''$  from the ROSAT-HRI cavity. In order to directly compare the *Chandra* image with the ROSAT image, we obtained an image in the 0.3 – 2 keV, which is approximately the band covered by ROSAT. This does not

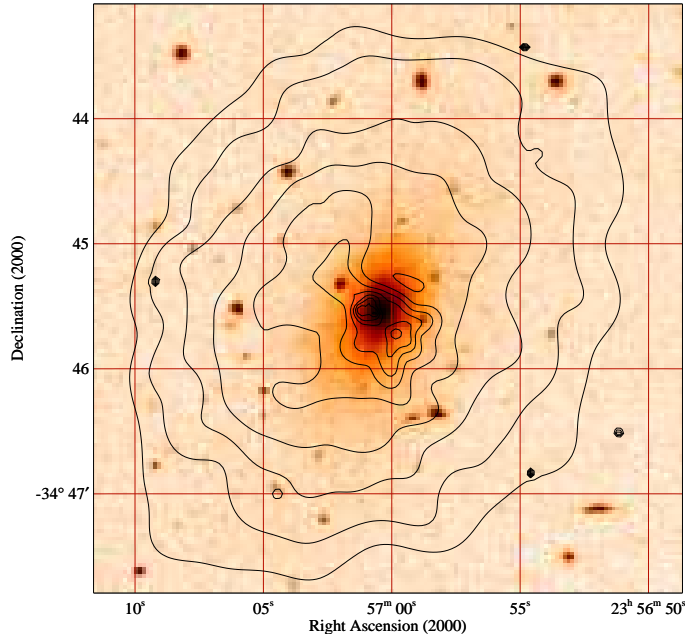


FIG. 1.—  $4\text{-}\sigma$  adaptively smoothed ACIS-S image (contours) overlaid on the Digitized Sky Survey image of A4059. See text for discussion.

change our conclusions regarding the position of the cavity and the discrepancy with ROSAT. Considering the unprecedented high spatial resolution and throughput of Chandra, we conclude that the SE cavity given by Chandra is likely to be real, not the result of statistical fluctuation (see Heinz et al. 2002). After an examination of the raw ROSAT data, we suggest that a  $3\sigma$  fluctuation in the photon statistics of the ROSAT image may have led to an incorrect determination of the SE cavity’s location. We also note that it is difficult to check the correctness of the ROSAT-HRI aspect solution given the lack of identifiable sources in this short observation.

As pointed out in Heinz et al. (2002), the axis connecting these two cavities lies perpendicular to the central hour-glass like structure but the center of the axis does not coincide with the radio galaxy (see Fig. 2 in § 3.2). Prompted mainly by that fact, Heinz et al. argued that the radio galaxy had interacted with a moving ICM and, hence, that the cavities had been “blown” in the north-east direction. As we show in § 3.4, spatially resolved X-ray spectroscopy, as well as the HST-WFPC2 image, provide further support for this hypothesis.

### 3.2. Radio morphology

Our new radio maps are presented in Fig. 2 as contours of flux density overlaid on an adaptively smoothed 0.3–8.0 keV ACIS image. It is interesting to compare this with the high-resolution 8.5 GHz and 4.8 GHz VLA/A- and B-array images of Taylor et al. (1994). While the radio emission at 8.5 GHz extends to the NW X-ray cavity and coincides with the deepest part of the cavity, it is not spatially coincide with the SE cavity (see Fig. 1 in Heinz et al. 2002). Our new CnB-array radio images show that the 1.4 GHz emission also does not extend into the SE cavity. Indeed, the radio axis does not seem to be aligned with the axis joining two X-ray cavities and there is no evidence for bending of the radio structure toward the direction of the two cavities. Below, we discuss the possibility that the X-ray cavities correspond to old radio lobes which have been

moved around by bulk ICM flows and may only be directly observable at low radio frequencies (100 MHz and below).

### 3.3. Optical Morphology

Figure 3 shows the HST/WFPC-2 image of the A4059 field. While an analysis of the optical galaxy cluster is beyond the scope of this paper, a large number of bright galaxies can be seen. By far the brightest, however, is the cD galaxy ESO349–G010 which has been placed on the PC-chip. The detailed high resolution PC image of ESO349–G010 is shown in Fig. 4. The most striking feature is the prominent dust lane that can be traced for at least 5 arcsec (corresponding to 5 kpc) projected across the central regions of the galaxy. The position angle of the dust lane is twisted by  $60 - 70^\circ$  relative to the radio axis of PKS2354–35, and coincides with the position angle of the bright SW ridge in the X-ray image. Similar dust lanes, also oriented roughly perpendicular to the radio axis, have been noted in HST data for the host galaxies of three Compact Symmetric Objects (CSOs) by Perlman et al. (2001). The Perlman et al. CSO-hosts also possess disturbed outer isophotes that suggest a significant merger event approximately  $\sim 10^8$  yr ago. Since it was taken as part of a snap-shot campaign, the data for ESO349–G010 lack the multi-band coverage and signal-to-noise to perform the Perlman et al. analysis.

### 3.4. Spatially-resolved X-ray spectroscopy

The X-ray morphology of the core of Abell 4059 is complex and asymmetric. Given the obvious lack of spherical symmetry (especially in the central regions of this system), any spatially-resolved spectral studies of this cluster will be subject to uncertain projection effects. With these caveats in mind, this section presents a detailed spatially-resolved spectroscopic investigation of Abell 4059.

#### 3.4.1. Adaptively binned image analysis

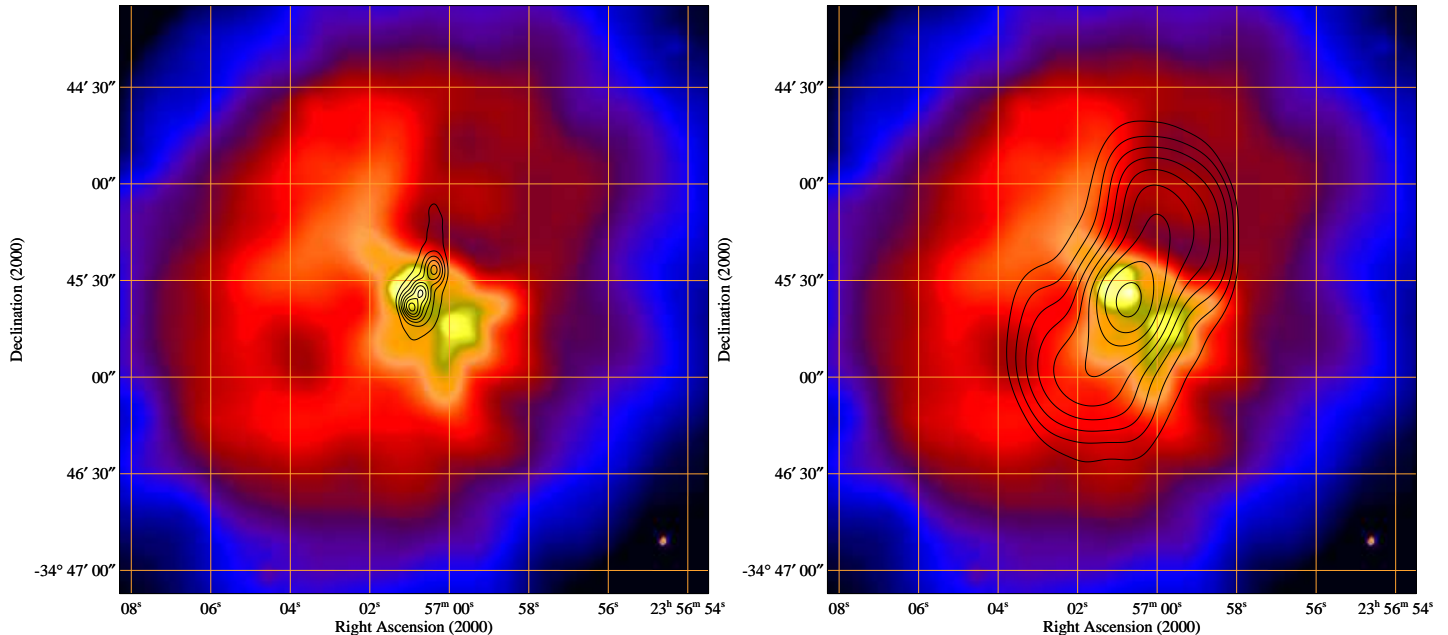


FIG. 2.— VLA/CnB-array images (contours) of A4059/PKS 2354-35 taken at 4.7 GHz (left panel) and 1.4 GHz (right panel) overlaid on the  $4\text{-}\sigma$  adaptively smoothed X-ray image.

Given the asymmetries present in the cluster core, we must analyze the spectral properties of the cluster across the 2-dimensional image. We achieve this using the “adaptive binning” method of Sanders & Fabian (2001). The adaptive binning code, kindly provided by Jeremy Sanders<sup>1</sup>, computes the optimal tiling across the image such that each tile possesses at least a specified number of photons. Spectra can then be extracted and analyzed for each tile. The major advantage of this method is that one can maintain high spatial resolution (i.e. small tiles) in the high count rate regions of the image.

The adaptive binning was set such that each tile possessed at least 600 counts, resulting in a fractional error on the net count rate of 0.04. Spectra and response matrices were extracted from each tile. Although an analysis using the 0.3 – 8.0 keV energy range could provide information on cold emission and intrinsic absorption in the cluster, such an analysis is severely hampered by calibration problems at the lowest energies, in particular the effects of contamination on the ACIS filter and charge-transfer inefficiency (CTI) in the CCD. Therefore, only data between 0.5 – 8.0 keV were included in this spectral analysis. The separate responses for each tile were weighted to account appropriately for instrumental response variations across the detector, using the `mkwarf` and `mkrmf` scripts implemented within CIAO. The original auxiliary response files created by CIAO tool `mkwarf` were corrected for degradation in the ACIS quantum efficiency (QE) using the software released by George Chartas and Konstantin Getman<sup>2</sup>. Background spectra were generated using the blank sky fields (Markevitch 2000) for the same part of the detector. All spectra were grouped to have at least 20 photons per energy bin, thereby facilitating the use of  $\chi^2$  fitting.

For our canonical spectral fits, each spectrum was modelled with a single temperature optically-thin thermal plasma component (modeled using the MEKAL model as implemented in

XSPEC; Mewe, Gronenschild & van den Oord 1985; Mewe, Lemen & van den Oord 1986; Kaastra 1992; Liedahl, Osterheld & Goldstein 1995) with a metallicity fixed at  $Z = 0.4$  and absorbed by the Galactic column density of  $N_H = 1.45 \times 10^{20} \text{ cm}^{-2}$ . Once we obtained the best-fit plasma emission measure and temperature for each bin, we derived the density, pressure and cooling time assuming that the plasma is single-phase and has a line-of-sight path length equal to the radial distance between the center of the bin and the center of the cluster (following the method of Fabian et al. 2001). We also studied the effect of relaxing the metallicity constraint and including the possibility of intrinsic absorption.

In Fig. 5, we show maps of the best fitting values of intrinsic absorption (for those fits that relax the absorption constraint), temperature, gas density, metallicity (for those fits that relax the metallicity constraint), pressure, entropy ( $s = p/n^{5/3}$ ), radiative cooling time and  $\chi^2_\nu$ . We have overlaid the X-ray contour map to facilitate comparison. Significant complexity can be seen in these maps. Within the centralmost regions of the cluster (about  $30''$  radius, see dotted circle contour in Fig. 5a), the gas density and pressure dramatically increase, reaching peak values of  $n_e \sim 0.11 \text{ cm}^{-3}$  and  $p \sim 2.7 \times 10^{-10} \text{ erg cm}^{-3}$ , and the temperature decreases reaching down to a value of  $kT \sim 1.4 \text{ keV}$ .

One of the most striking and unusual features within the core of Abell 4059 is the the bright ridge of emission stretching from the cluster core to the SW. Our temperature map (Fig. 5b) clearly shows that the ridge is composed of gas that is cool (with a temperature of  $\sim 1.4 \text{ keV}$ ) and has low entropy. In order to investigate the spatial differences in the properties of X-ray emitting gas in and around this structure, Fig. 6 shows the best fitting parameters for the tile fits, averaged in radial bins, as a function of the distance from the center of the cluster. Fig. 6 distinguishes between the NE and SW sides of the cluster in

<sup>1</sup><http://www-xray.ast.cam.ac.uk/jss/adbin/>

<sup>2</sup><http://www.astro.psu.edu/users/chartas/xcontdir/xcont.html>

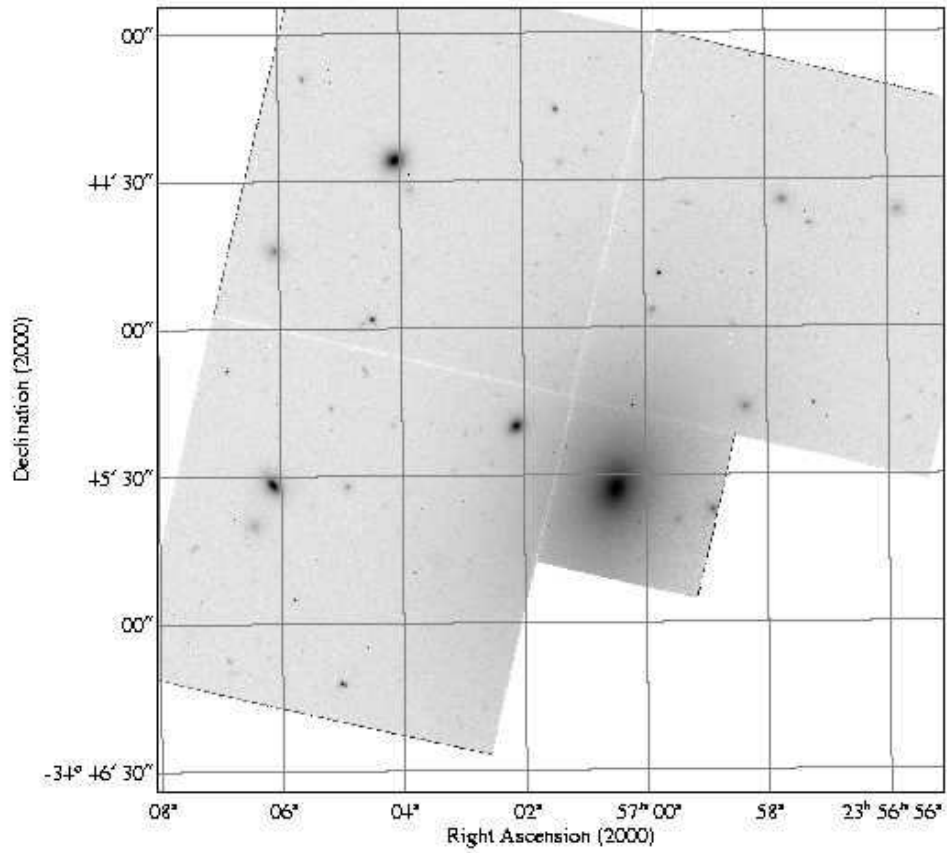


FIG. 3.— HST-WFPC-2 image of the A4059 field (see §2.3 for details of the observation). The cD galaxy ESO349-G010 is clearly visible on the PC-chip.

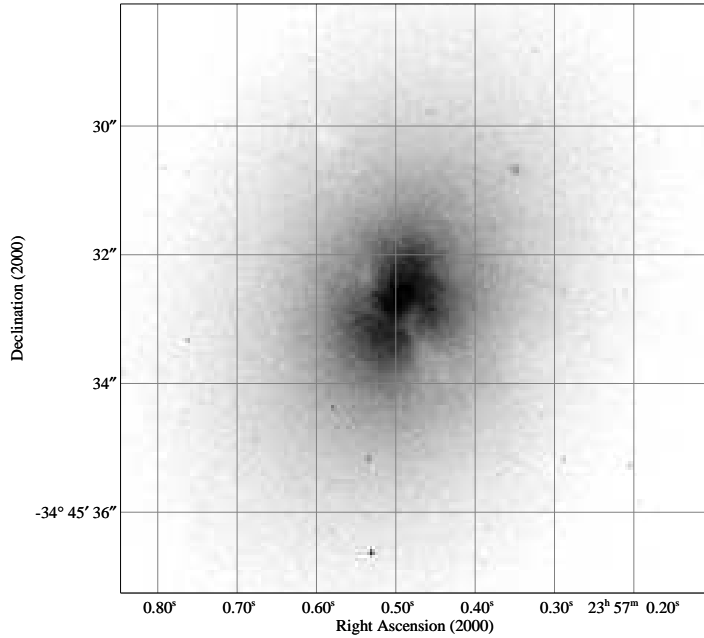


FIG. 4.— WFPC-2 imaging of the cD galaxy ESO349-G010, the host galaxy of the radio source PKS2354-35 (see §2.3 for details of the observation). Note the prominent dust lane crossing the galaxy from the north-east to the south-west.

FIG. 5.— Maps of column density (panel a), temperature (panel b), gas density (panel c), metallicity (panel d), pressure (panel e), specific entropy (panel f), cooling time (panel g), and the appropriated reduced  $\chi^2$  value (panel h) for adaptively binned central 2.5' image of A4059, with an intrinsic absorption single temperature MEKAL model. Dotted circle contour ( $r < 25$  kpc) includes the bright hour-glass like structured region of the cluster.

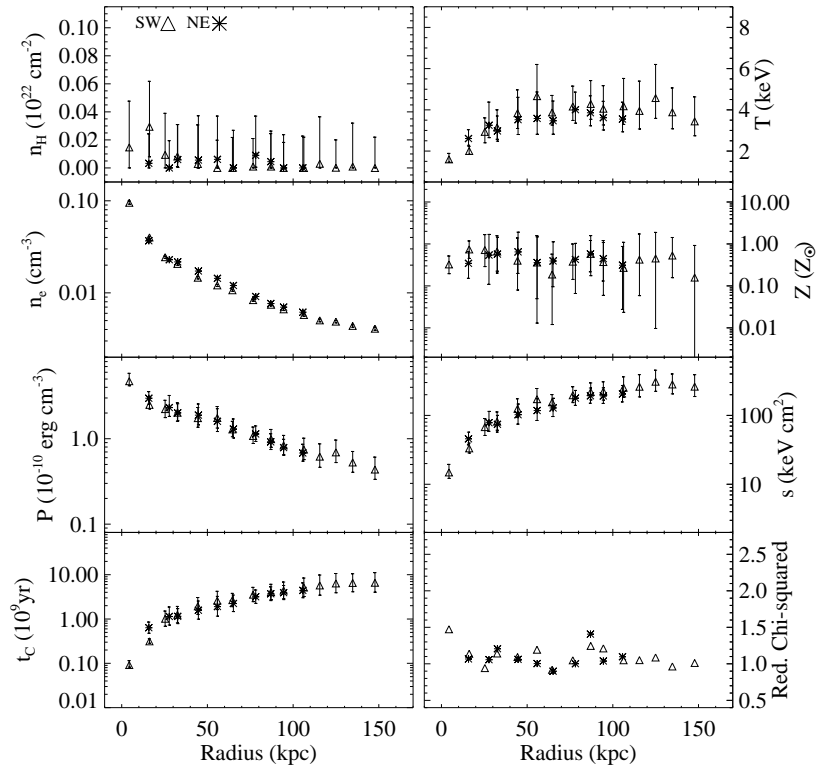


FIG. 6.— Radial distribution of the fitted parameters for the bins in Fig. 5 with 1- $\sigma$  errors. Each profile corresponds to the fitted values of NE and SW sides of the cluster center. The radius is the mean distance from the cluster center to the each bin.

order to study the nature of the bright SW ridge. The most significant result from Fig. 6 is that the radiative cooling time

within the ridge is rather small (less than 1 Gyr within 25 kpc

and about 0.1 G yr within the innermost few kpc).

The temperature and pressure maps in Fig. 5b and 5e exhibit no evidence for any hot gas in or around the cavities. We can see that the SW part adjacent to the central hour-glass like structure shows obviously sharp gradients in the fitted temperature, entropy, and radiative cooling time maps, while the NE shows a rather smooth profile. The oscillation of fitted values shown in Fig. 6 results from this non-axisymmetric feature.

### 3.4.2. Detailed X-ray spectral study of annuli

Motivated by the above analysis, we have examined the spectra for annular regions in the cluster. Source spectra, background spectra, response matrices and ancillary files were generated for each annular region, as in § 3.4.1. Finally, the spectra were binned so as to possess a minimum of 20 counts per bin, thereby allowing the use of  $\chi^2$  fitting techniques. We fitted each spectrum to a variety of models in the energy range of 0.8–8.0 keV<sup>3</sup>: a single-phase emission model and two multi-phase emission models. For a single-phase emission model (hereafter, model-S), the spectrum is fitted with single-temperature MEKAL model, and for multiphase emission models, with two-temperature MEKAL model (model-T) or a single temperature plasma plus cooling flow model (model-SCF). In the cooling flow model, we set the upper (initial) temperature of the cooling material to be equal to the temperature of the single plasma component. The lower “cutoff” temperature of the cooling flow model is set to 0.1 keV (i.e., significantly below our bandpass). In this analysis, the intervening neutral absorption column density is left as a free parameter. For reference, the Galactic absorption column density is  $N_{\text{H,Gal}} = 1.45 \times 10^{20} \text{ cm}^{-2}$ .

The results of this analysis are shown in Fig. 7, together with the 90% confidence ranges for one interesting degree of freedom ( $\Delta\chi^2 = 2.7$ ). Here, we report the results for both the fixed abundance fits (open squares) and variable abundance fits (diagonal crosses).

When fitted with a single temperature component plasma model (parameterized by a single temperature and a single emission measure; Fig. 7a), some clear trends are seen. The temperature decreases from 4 keV in the outer regions of the cluster to 2 keV in the central regions. When applying model-S with metallicity as a free parameter, we find an enhanced metallicity (approaching almost cosmic abundances) at intermediate radii (20–50 kpc), with metallicities decreasing to 0.4–0.5  $Z_{\odot}$  of the cosmic value at smaller and large radii. The goodness-of-fit is, however, rather poor when applying model-S to the cluster center. Much of the poor goodness of fit is due to an underprediction of the soft flux by the single temperature model. It is this mis-match that is responsible for the unphysically small absorption (i.e. less than  $N_{\text{H,Gal}}$ ) implied by these fits.

The two temperature model (model-T; Fig. 7b) is a much better description of the spectral data, especially within the inner 50 kpc. The actual values of the two temperatures seem to be weak functions of radius, with  $kT_{\text{high}} \approx 4 - 5 \text{ keV}$  and  $kT_{\text{low}} \approx 1 - 2 \text{ keV}$  in most of the radial bins. Apparent exceptions to this are the 20–40 kpc radial bins which, in the fixed abundance fits, both appear to have  $kT_{\text{high}} > 7 \text{ keV}$ . However, variable abundance fits suggest that the abundance strongly deviates from  $Z = 0.4Z_{\odot}$  at these radii and, once that is accounted for, the upper plasma temperature is also approximately 4 keV. The principal qualitative difference between the

one and two temperature fits lies in the abundance profile. In the one temperature fits, there is a pronounced drop in the metallicity as one proceeds from 30 kpc into the center of the cluster. On the other hand, the two temperature fits show a jump in the metallicity at about 40 kpc, with the metallicity displaying an approximately flat radial dependence within this radius. Thus, the metallicity peak noted in the single temperature fits is probably an artifact of the model (also see case of the Virgo Cluster, Molendi & Gastaldello, 2001). Due to the better quality of these fit (especially in the soft band), the measured absorption column is more meaningful for model-T. We see that all radii are consistent with Galactic absorption, i.e., there is no evidence for intrinsic absorption in this cluster.

The cooling flow model (model-SCF) is a poorer description of these data than the two temperature model (model-T). This is due to the fact that the model includes gas at all temperature from the ambient temperature down to 0.1 keV whereas, as noted in the introduction, the cooling in many clusters (including A4059; Peterson et al. 2003) is truncated at 1–2 keV by some process. With this caveat, we note that the cooling flow model reproduces the temperature structure of model-S and the metallicity behaviour of model-T.

### 3.4.3. Deprojection analysis

Of course, the analysis presented in the previous section has not attempted to correct for projection effects; the observed emission from a particular annulus contains all of the projected foreground and background emission, thereby complicating the interpretation of these results.

To address this complication, we have performed a spectral analysis of “deprojected” spectra. In detail, we deproject the cluster emission into eight shells assuming spherical symmetry using the `project` model within the XSPEC spectral fitting package<sup>4</sup>. Clearly, any simple symmetry assumption will break down in the morphologically complex inner regions of A4059. However, we might hope to perform a deprojection analysis of this cluster beyond 30 – 40 kpc, where it is fairly regular.

With this deprojection in hand, we initially model the spectrum of each shell with an absorbed one-temperature mekal model in which the global abundance is a free parameter. The density of the plasma is determined from the plasma emission measure assuming that the plasma uniformly fills the volume of the shell. These results are reported in Fig. 8a; for comparison, we also show the results from fitting model-S to the spectra from the projected annuli (naively computing the density from the observed emission measure of the annulus). It can be seen that the single-temperature deprojection study reproduces the peak in metallicity at 30–40 kpc. Within this radius, the spherical assumption clearly breaks down and hence the deprojection is not to be trusted. Indeed, the leveling off of the ICM density, and the drop in ICM pressure within the centralmost bin is unphysical and almost certainly due to the morphological complexities associated with the radio-galaxy/ICM interaction.

In order to examine the possibility of multiphase gas, we add an additional temperature component to those deprojected spectra for which it is a significant improvement in the goodness of fit (employing the F-test with a 90% level confidence threshold). Only the inner two radial shells required a second temperature component (Fig. 8b). As in the case of the projected study, the

<sup>3</sup>Note that a more stringent lower-limit on the energy band (0.8 keV) is used in this analysis as compared with the adaptive-binning analysis presented above. This is to secure against calibration issues in these higher signal-to-noise spectra.

<sup>4</sup>Note that we use the latest version of `project` that can correctly handle the multiple datasets.

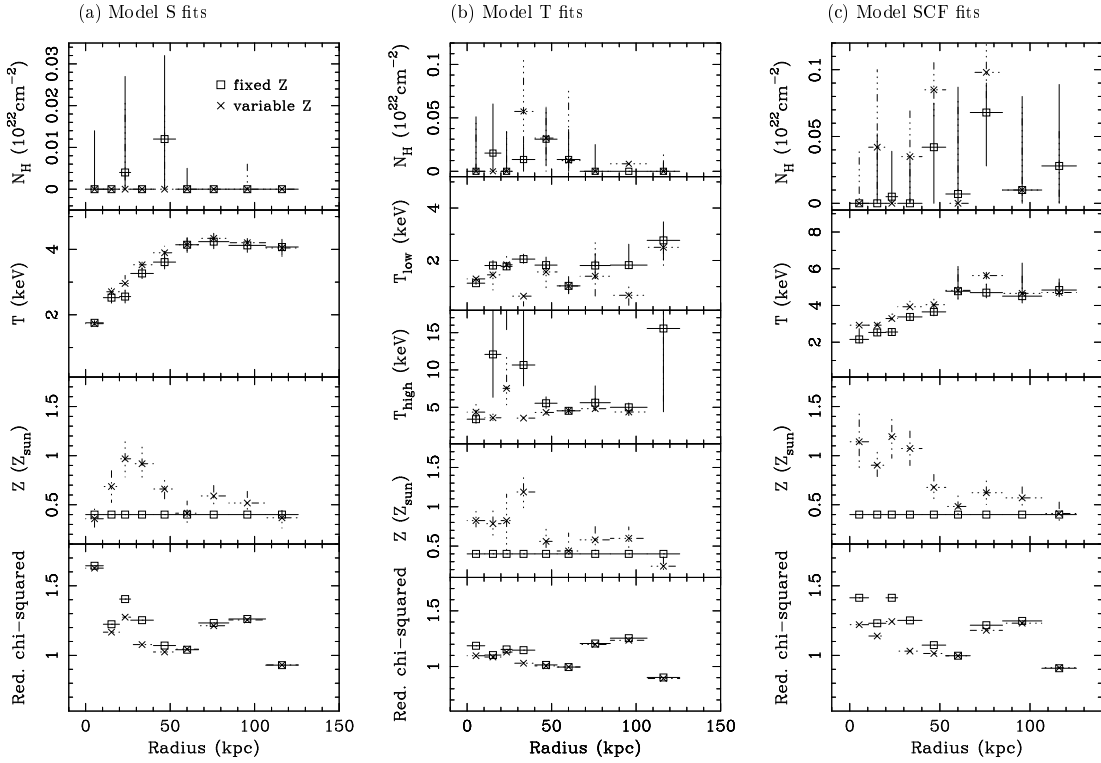


FIG. 7.— Temperature, absorbing column density, metallicity, and the appropriate reduced  $\chi^2$  value as a function of radius fitted with the single temperature MEKAL model (model-S; panel a), two temperature MEKAL model (model-T; panel b), and single temperature plasma plus cooling flow model (model-SCF; panel c). Error bars are shown at the  $1\text{-}\sigma$  level for one interesting parameter ( $\Delta\chi^2 = 1$ ). Open square and cross show the results with metallicity fixed to the 0.4 times solar value and with metallicity free, respectively. For model-T, the metallicities of the two phases were fixed to be same.

central metallicity drop is removed by the addition of a second component.

#### 4. DISCUSSION AND CONCLUSIONS

##### 4.1. Summary of observational results

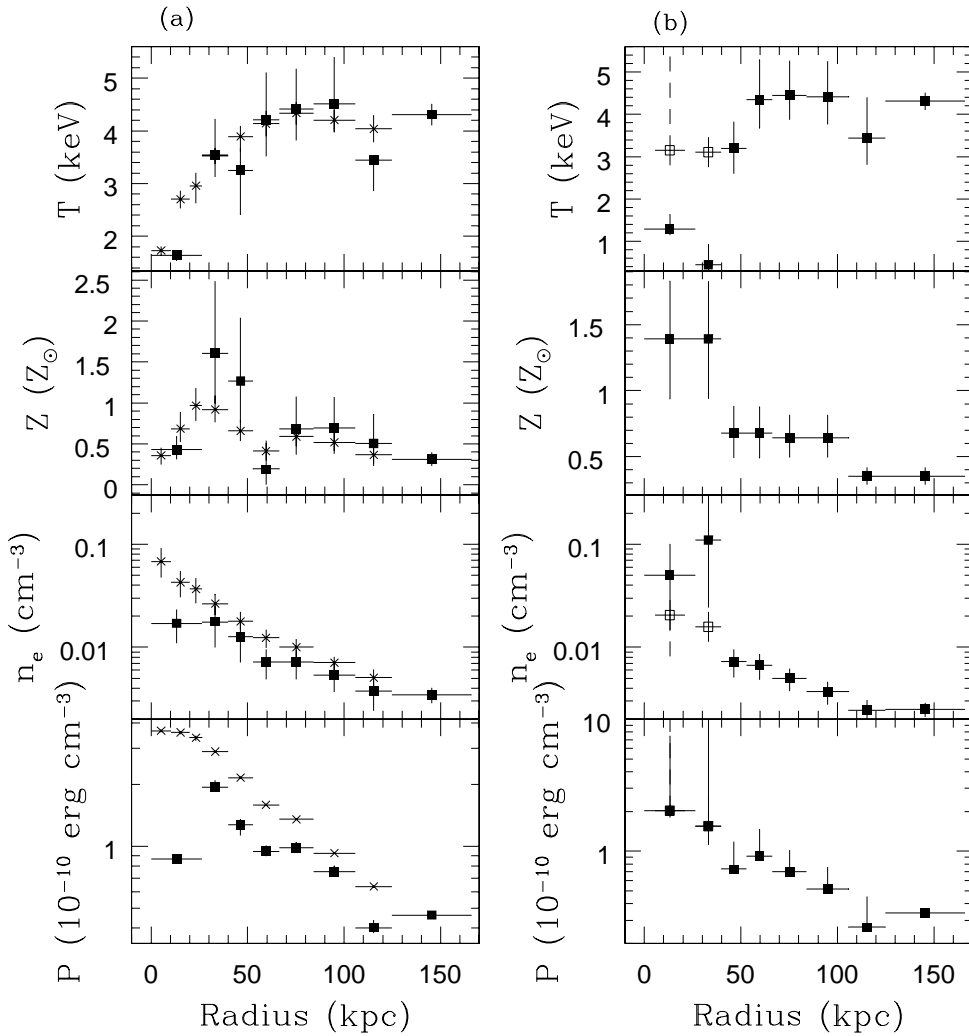


FIG. 8.— Deprojection analysis of the *Chandra*/ACIS-S data for A4059. Panel (a) shows the results of fitting a single temperature plasma to the spectrum from each shell (filled squares), with the density determined from the emission measure assuming that the plasma uniformly fills the volume of the shell. The crosses show the results from the (projected) annular study of Section 3.4.2, with the density naively determined from the emission measure. In panel (b), an additional plasma component has been included in the deprojected study in those bins for which it makes a significant improvement to the goodness of fit (i.e., the inner two bins). It is assumed that the two components are in pressure equilibrium, have the same metallicity, and jointly fill the volume of the shell.

There is clear evidence of a vigorous and complex radio-galaxy/cluster interaction between PKS2354–35 and A4059. Prior to the analysis presented in this paper, the known facts relevant to this interaction were:

1. There are two large ICM cavities approximately aligned with the axis of the radio galaxy. Huang & Sarazin (1998) and, later Heinz et al. (2002), showed that the radio source, as defined in the A- and B- array 4.8 GHz and 8.5 GHz VLA observations of Taylor et al. (1994) extends into the NW cavity, but does not extend to (or even point at) the SE cavity.
2. There is an offset between the center of the axis connecting the two cavities and the galactic nucleus. One is given the impression that, assuming the cavities were created symmetrically by the radio galaxy, they have subsequently “drifted” in a NE direction.
3. There is a bright ridge of emission extending from the

center of the cluster in the SW direction. This ridge terminates about 25 kpc to the SW of the center in an abrupt edge.

To this, we can now add the following informations:

1. VLA/CnB-array data taken at 1.4 GHz, which is much better matched to detecting arcmin-scale structures than the previous radio data, still fails to detect any radio emission associated with the SE X-ray cavity.
2. There is no indication that the gas around the X-ray cavities is any hotter or higher entropy than the ambient gas. In other words, there is no evidence for a strong (or even moderately weak) shock surrounding the X-ray cavities.
3. The SW ridge appears to be in approximate pressure balance with the ambient material and is X-ray bright because of its lower temperature and higher density. The

radiative cooling time in this structure is much shorter than that of the surrounding ICM, becoming as short as 100 Myr (compared with a general “core” cooling time of greater than 500 Myr).

4. There is a robust metallicity gradient within the cluster, with high metallicity (approaching solar) in the cluster center and then declining by a factor of 2 beyond 50 kpc. This is reproduced in both the annular (i.e. projected) and deprojected spectral study. The presence of a central depression in the metallicity profile is suggested by single temperature fits to either the projected or deprojected spectra. However, the reality of this feature is unclear (see above for details).
5. HST/WFPC-2 imaging reveals that the cD galaxy and host of PKS2354–35, ESO349–G010, displays a prominent 5 kpc dust lane oriented roughly perpendicular to the radio-axis. This suggests that it has accreted a dust rich companion galaxy in the past  $10^8$  yr or so.

In this section, we discuss the constraints that these observations place on the nature of the interaction.

#### 4.2. *Inflating the cavities*

As discussed in Heinz et al. (2002), the current radio source is likely too weak to produce notable cavities, and it is likely that the observed ICM cavities are “ghosts” of a previous and more powerful period of activity. In this picture, the cavities are in a passive phase of evolution (see Reynolds, Heinz & Begelman 2002). The X-ray cavities, which were created by a past phase of supersonic lobe expansion, have decelerated to sub-sonic velocities. Any shocks once bounding the lobes have weakened into mere compression waves. The fact that this activity produces an expanding shell of ICM implies that gas from the core regions will be lifted to higher points in the cluster, thereby adiabatically cooling as it de-pressurizes. This cooling effect can largely offset the heating from the ICM compression and (certainly to within the accuracy of our data) mask any remaining signs of compressional heating. This explains the lack of hot gas in or around the cavities.

In this evolutionary phase, the cavities will buoyantly rise within the cluster potential on a timescale a factor of a few longer than the sound crossing time of  $\sim 2 \times 10^7$  yrs. As they rise buoyantly and expand, the relativistic electron population will undergo synchrotron, inverse Compton, and adiabatic energy losses. The synchrotron and inverse Compton losses result in a high-frequency cut-off that gradually marches to lower and lower radio frequencies. Using the standard formulae for synchrotron losses (e.g., Rybicki & Lightman 1979), it is readily shown that, assuming an isotropic relativistic electron distribution evolving in a constant or decreasing strength magnetic field, the high-frequency cut-off of the synchrotron spectrum will obey

$$\nu_{\text{cut}} \lesssim 26 \left( \frac{B}{60 \mu\text{G}} \right)^{-3} \left( \frac{t}{20 \text{Myr}} \right)^{-2} \text{ MHz}, \quad (1)$$

where approximate equality corresponds to the case where the magnetic field and the particle pressure are constant in time. This expression assumes no fresh injection or acceleration of relativistic electrons (which would turn the cut-off into a spectral break), and hence only applies once the radio-lobes are no longer supplied by active jets (i.e., after the radio-source

“dies”). The ICM pressure at the location of the ghost-cavities is measured to be approximately  $p \approx 10^{-10}$  ergs  $\text{cm}^{-3}$ . If we assume that the synchrotron emitting plasma is in pressure equilibrium with the surrounding ICM (which is very likely to be true for the ghost cavities) and furthermore, that the magnetic field in the plasma has approximately equipartition strength and is tangled on scales small compared to the cavity size, this pressure gives us a field strength of  $B \approx 60 \mu\text{G}$ . Thus, assuming ICM/cavity pressure balance and equipartition magnetic fields, we can see from eqn.(1) that the cavities will fade out of the 1.4 GHz band only 4 Myr or so after the outburst of the radio-galaxy activity has ceased. Since we believe the ghost cavities to be approximately 20 Myr old (Heinz et al. 2002), we see that there has been ample time for the plasma filling the cavities to fade out of the higher frequency radio bands *if the magnetic field possesses roughly equipartition strength*.

Studies with ROSAT, *Chandra*, and *XMM-Newton* have allowed the magnetic field strengths of several radio lobes to be estimated through the direct detection of the X-rays thought to be produced by inverse Compton scattering of the Cosmic Microwave Background (CMB) by the relativistic electrons (Leahy & Gizani 2001; Hardcastle et al. 2002; Grandi et al. 2003; see also Wilson, Young, & Shopbell 2001 for related arguments in the hot spots of Cygnus A). In these studies, it is typically found that the magnetic field is at least a factor of two lower than the equipartition value. Even if the magnetic field has half of the equipartition field strength, there is sufficient time for the 1.4 GHz emission from the ghost cavities to fade.

Having put forward a fairly traditional hypothesis for the formation and evolution of the X-ray cavities, we now proceed to consider the complexities special to Abell 4059.

#### 4.3. *Possible formation mechanisms for the SW ridge*

One of the most striking feature in the X-ray morphology of A 4059 is the bright and cool SW ridge. The SW edge of this ridge appears to be surface across which the temperature and entropy of the gas change significantly with little or no change in pressure. In many ways, this is similar to the “cold fronts” that have been observed in many clusters (Markevitch et al. 2000; Vikhlinin, Markevitch & Murray 2001). Here, we will discuss four possible formation mechanisms for this structure.

##### 4.3.1. *A cool disk associated with a rotating cooling flow*

Huang & Sarazin (1998), who were the first to note the SW ridge using ROSAT HRI data, suggested that it might be the rotationally-supported disk of cooled gas expected to form at the center of a rapidly-rotating cooling flow. The notion that such a disk-like structure can form in high angular momentum cooling flows has gained support from axisymmetric hydrodynamically simulations (Garasi et al. 1998), although there are still unresolved questions as to the effect that turbulent angular momentum transport may have on the formation and stability of such disks (Nulsen, Stewart, & Fabian 1984).

However, it is clear from the high-resolution *Chandra*-ACIS data that the SW ridge does *not* extend NE of the cluster center, i.e., it is one-sided. This can be seen in both the total intensity map (Fig. 1) and, more clearly, in the temperature map (Fig. 5b). This runs counter to the idea that the SW ridge is part of a large ( $\sim 20$  kpc) disk at the center of the cluster. Thus, just on the basis of morphology, we can reject the hypothesis that this structure is part of a disk associated with a rotating cooling flow.

#### 4.3.2. *Cool wakes of buoyantly rising radio plumes*

Numerical simulations of the buoyant phase of a radio-galaxies evolution show that appreciable amounts of ICM from the cluster core can become entrained in the “wake” of a buoyantly rising plume of radio plasma (Brüggen et al. 2002; Reynolds, Heinz, & Begelman 2002). This material adiabatically decompresses and cools as it is dragged upwards in the cluster potential, and would appear as distinct filaments of cold and dense material strung out along the path of the buoyant plume.

As discussed by Young, Wilson & Mundell (2002), these wakes of cold gas are probably responsible for the arc-like feature seen in *ROSAT*-HRI and *Chandra*-ACIS observations of M87 and the core of the Virgo cluster. This structure is composed of narrow filaments or columns of cold gas (with  $kT \sim 1$  keV, compared with  $kT \sim 3$  keV for the surrounding ICM), probably in pressure equilibrium with their surroundings, that extend for 2–3 arcmins East and South-West of M87. They are coincident with, but more more narrowly confined than, the 90 cm radio arc observed by Owen, Eilek & Kassim (2000). This supports the idea that the filament has been entrained and pulled out of the central parts of M87/Virgo by a buoyantly rising plume.

However, it seems unlikely that such a model can explain the SW ridge of A 4059. There is no indication of any radio-lobe (even a very old one) in the SW direction, i.e., there is no radio emission and no ICM cavity in that quadrant of the cluster. Furthermore, the SW ridge does not take on the form of a narrow filament reaching out from the cD galaxy, as would be expected for wake material on the basis of both the numerical simulations and the Young et al. (2002) observations of Virgo. Instead, the SW ridge is a rather broad and flaring feature extending from the cD galaxy. On the basis of these two observations, we reject the hypothesis that the SW ridge corresponds to cool material that has been entrained in the wake of a buoyantly rising plume of radio-plasma.

#### 4.3.3. *The accreted core of a cooler sub-cluster*

The discovery of a large dust lane in the HST-WFPC2 image of ESO349-G010 suggests the accretion of a dust and gas rich companion galaxy within the past  $10^8$  yrs. It is possible that this galactic-merger event was actually the late stages of the merger of a smaller galaxy cluster or group with A 4059. In this case, one may attempt to identify the SW ridge with the remnant ICM core of the minor cluster. The well known correlation between the X-ray luminosities and temperatures of galaxy clusters and groups,  $L \sim T^3$ , means that the accreted minor system is likely to possess an ICM that is significantly cooler than the ambient temperature of A 4059 ( $kT \sim 4$  keV). We note that similar ideas have been proposed to explain the cold fronts observed in other clusters (Markevitch et al. 2000; Bialek, Evrard & Mohr 2002; Nagai & Kratsov 2002).

However, this scenario may be problematic for the case of A 4059 (although it may well explain some of the classical cold fronts seen in other clusters). While it is true that the ICM temperature of the accreted subcluster may initially be cooler than that of A 4059, it will compress and heat as it enters the higher pressure environment of the richer cluster. The relevant thermodynamic quantity to consider is the *entropy* of the ICM cores of A 4059 and the accreted cluster. In fact, for clusters of the mass of A 4059 and smaller, the entropy of the ICM core is almost constant from one cluster to another (Lloyd-Davies,

Ponman & Cannon 2000; Mushotzky et al. 2003). Thus, even if it evolved adiabatically, the ICM-core of the accreted group would be compressionally heated to approximately the ambient temperature of A 4059. Any departure from adiabatic evolution (e.g., the effects of shocks) will only increase the entropy and temperature of the accreting ICM. In order to produce a colder region, radiative cooling needs to dominate the evolution of the accreted core. While this may be true, either fine tuning or significant feedback (either via conduction or radio-galaxy heating) is needed to prevent the core from cooling completely.

#### 4.3.4. *A compression front associated with bulk ICM motion*

The apparent displacement of the center of the cavities from the cluster center and the different position angle between the extended radio emission and the cavities suggests bulk motion of the ICM flow. Noting that the line connecting the centers of the two cavities misses the radio-galaxy core by approximately 10 arcsec, corresponding to 10 kpc, we can use estimates of the age of the radio source ( $\sim 20$  Myr; Heinz et al. 2002) to estimate that the ICM is flowing past the cD galaxy at a velocity of  $500 \text{ km s}^{-1}$  projected onto the plane of the sky. The different position angle between the axis connecting the ghost cavities and the current extended radio emission demands either a change in the radio-axis itself, or some rotation in the ICM flow. Both numerical simulations (e.g., Roettiger, Loken & Burns 1997) and *Chandra* observations (e.g., Markevitch et al. 2003) suggest this kind of large scale ICM “sloshing” can readily occur after a major cluster merger.

In this picture, the bright and cool SW ridge is located at the position where we expect the radio-galaxy induced expanding ICM shell to be maximally compressed by the ICM flow. The sharp SW edge of this feature is readily interpreted at the interface between the ambient ICM (which we suppose is flowing in a NE direction) and the expanding ICM shell formed by the same period of radio-galaxy activity that formed the X-ray cavities.

One might expect that such compression would heat this material, contrary to observations. However, the fact that the cooling time of the ridge material is small demands that we consider radiative cooling effects. In the simplest case of adiabatic compression in the bremsstrahlung regime, the cooling time is proportional to  $n^{-2/3}$ . Hence, a weak shock will slightly reduce the cooling timescale. Radiative cooling can be further aided by the kinematics of the radio-galaxy/cluster interaction, which keeps this material in the high pressure regions of the cluster core for longer. Even given this, there appears to be a fine tuning problem; it is difficult to explain the cooling of the SW ridge unless it was on the verge of undergoing dramatic radiative cooling anyways. A detailed exploration of these hydrodynamical and radiative questions will be deferred until future publications.

#### ACKNOWLEDGMENTS

We thank Mitchell Begelman, and Andy Young for stimulating conversations throughout the course of this work. We are also grateful to the anonymous referee for comments that significantly improved the paper. This work was supported by SAO grant GO0-1129X (YC), the National Science Foundation grant AST0205990 (CSR), and Korea Research Foundation grant KRF 2001-041-D00052(JY). Additional support for this work (SH) was provided by the National Aeronautics and Space Administration through Chandra Postdoctoral Fellowship Award Number PF3-40026 issued by the Chandra X-ray

Observatory Center, which is operated by the Smithsonian Astrophysical Observatory for and on behalf of the National Aero-

navics Space Administration under contract NAS8-39073.

#### REFERENCES

- Bialek J.J., Evrard A.E., Mohr J.J., 2002, ApJ, 578, L9  
 Blanton, W.L., Sarazin, C.L., McNamara, C.L., & Wise, M.W., 2001, ApJL, 558, L15  
 Böhringer, H., Nulsen, P.E.J., Braun, R., & Fabian, A.C., 1995, MNRAS, 274, L67  
 Brüggen, M., Kaiser, C.R., Churazov, E., & Ensslin, T. A., 2002, MNRAS, 331, 545  
 Clarke, D., Harris, D.E., & Carilli, C.L., 1997, MNRAS, 284, 981  
 David, L. R. et al., 2001, ApJ, 557, 546  
 Fabian, A.C., 1994, ARA&A, 32, 277  
 Fabian, A.C., Mushotzky, R.F., Nulsen, P.E.J., & Peterson, J.R., 2001, MNRAS, 321, L20  
 Fabian A.C., Voigt L.M., Morris R.G., 2002, MNRAS, 335, L71  
 Fabian, A. C. et al., 2000, MNRAS, 318, L65  
 Garasi, C., Loken, C., Burns, J.O., & Roettiger, K., 1998, MNRAS, 298, 697  
 Grandi P. et al., 2003, ApJ, 586, 123  
 Hardcastle M.J., Birkinshaw M., Cameron R.A., Harris D.E., Looney L.W., Worrall D.M., 2002, ApJ, 581, 948  
 Heinz, S., Reynolds, C.S., & Begelman, M.C., 1998, ApJ 501, 126  
 Heinz, S., Choi, Y.-Y., Reynolds, C.S., & Begelman, M.C., 2002, ApJ, 569, L79  
 Huang, Z., Sarazin, C.L., 1998, ApJ, 496, 728  
 Kaastra J.S., 1992, An X-ray Spectral Code for Optically-Thin Plasmas (Internal SRON-Leiden Report, updated version 2.0)  
 Jones, C. et al., 2002, ApJ, 567, L115  
 Leahy J.P., Gizani N.A.B., 2001, ApJ, 555, 709  
 Liedahl D.A., Osterheld A.L., Goldstein W.H., 1995, ApJL, 438, 115  
 Lloyd-Davies, E.J., Ponman, T.J., & Cannon, D.B. 2000, MNRAS, 315, 689  
 Markevitch M. et al., 2000, ApJ, 541, 542  
 Markevitch M. et al., 2002, ApJ, 586, L19  
 Mewe R., Gronenschild E.H.B.M., van den Oord G.H.J., 1985, A&AS, 62, 197  
 Mewe R., Lemen J.R., van den Oord G.H.J., 1986, A&AS, 65, 511  
 McNamara, B. R. et al., 2000, ApJL, 534, L135  
 McNamara, B. R. et al., 2001, ApJ, 562, 149  
 Molendi S., Gastaldello F., 2001, A&A, 375, L14  
 Mushotzky, R.F., to appear in "Emergence of Cosmic Structure", eds. S.S.Holt & C.S.Reynolds, (AIP conf.)  
 Nagai D., Kratsov A., 2002, 587, 514  
 Nulsen, P.E.J., Stewart, G.C., & Fabian, A.C., 1984, MNRAS, 208, 185  
 Nulsen, P.E.J., David, L.P., McNamara, B.R., Jones, C., Forman, W.R., & Wise M., 2002, ApJ, 568, 163  
 Owen, F.N., Eilek, J.A. & Kassim, N.E., 2000, ApJ, 543, 611  
 Reynolds, C.S., Heinz, S., & Begelman, M.C., 2001, ApJL, 549, L179  
 Reynolds, C.S., Heinz, S., & Begelman, M.C., 2002, MNRAS, 332, 271  
 Roettiger K., Loken C., Burns J.O., 1997, ApJS, 109, 307  
 Ruszkowski M., Begelman M.C., 2002, ApJ, 581, 223  
 Rybicki, G.B., Lightman, A.P., 1979, *Radiative Processes in Astrophysics*, Wiley  
 Peterson, J.A. et al., 2001, A&A, 365, 104  
 Peterson, J.A., et al., 2003, ApJ, 590, 207  
 Sanders, J.S., Fabian, A.C., 2001, MNRAS, 325, 178  
 Tamura, T. et al., 2001, A&A, 365, L87  
 Taylor, G.B., Barton, E.J., & Ge, J.P., 1994, AJ, 107, 1942  
 Vikhlinin A., Markevitch M., Murray S.S., 2001, ApJ, 549, L47  
 Voigt L.M., Schmidt R.W., Fabian A.C., Allen S.W., Johnstone R.M., 2002, MNRAS, 335, L7  
 Wilms, J., Allen, A., McCray, R., 2000, ApJ, 542, 914  
 Wilson A.S., Young A.J., Shoppell P.L., 2001, ApJ, 547, 740  
 Young, A.J., Wilson, A.S., & Mundell, C.G., 2002, ApJ, 579, 560

This figure "fig5.jpg" is available in "jpg" format from:

<http://arxiv.org/ps/astro-ph/0402131v1>